J Solid State Electrochem (2017) 21:2555–2566
DOI 10.1007/s10008-016-3457-3

ORIGINAL PAPER

α-Fe_2O_3 thin films by liquid phase deposition: low-cost option for supercapacitor

Shreelekha N. Khatavkar[1] · **Shrikrishna D. Sartale**[1]

Received: 6 October 2016 / Revised: 26 October 2016 / Accepted: 31 October 2016 / Published online: 12 November 2016

Abstract In the present study, iron oxide (α-Fe_2O_3) thin films with good adhesion on stainless steel substrates are deposited by liquid phase deposition (LPD) technique, which is additive and binder-free. Iron oxyhydroxide (FeOOH) thin films are formed by means of a ligand-exchange equilibrium reaction of metal-fluoro complex ions and an F^- ions consuming reaction by using boric acid (H_3BO_3) as a scavenging agent. These films are annealed at 500 °C to get α-Fe_2O_3 thin films. The transformation from hydrophobic to hydrophilic nature of the films is observed due to annealing. The films are characterized by different techniques. The α-Fe_2O_3 film is checked for electrochemical supercapacitive performance in Na_2SO_3 solutions of various concentrations. Specific capacitance is calculated from cyclic voltammetry at numerous scan rates (5–200) mV s^{-1}. The highest obtained value of specific capacitance is 582 F g^{-1} at 5 mV s^{-1} for 0.5 M Na_2SO_3 electrolyte. The maximum values of specific power and specific energy are 6.9 and 53.4 Wh kg^{-1} from the charge-discharge curve at the current density 2 mA cm^{-2} in 0.5 M Na_2SO_3 electrolyte.

Keywords Hematite · LPD · Thin films · Supercapacitor

Electronic supplementary material The online version of this article (doi:10.1007/s10008-016-3457-3) contains supplementary material, which is available to authorized users.

✉ Shrikrishna D. Sartale
sdsartale@physics.unipune.ac.in

[1] Thin Films and Nanomaterials Laboratory, Department of Physics, Savitribai Phule Pune University, Pune 411007, India

Introduction

Today, every corner of the world is facing the problem of energy crisis. Hence, there is need of sustainable energy sources and storage devices. The typical non-conventional energy devices such as batteries, fuel cells and supercapacitors are based on the principle of electrochemical energy conversion [1]. As long as the fuel is fed, the electrical energy can be obtained from a fuel cell. Whereas, as per requirement, the stored energy can be drawn from a battery. Supercapacitors are fabricated to bridge the gap between batteries and capacitors to form fast charging energy storage device of intermediate specific energy [2]. Supercapacitor is a device for energy storage which possess high specific capacitance, power density and long cycle life [3]. Electrochemical supercapacitor (EC) stores a lot of energy in a small volume and releases it in the form of power. There are two types of ECs based on the electrochemical mechanisms of energy storage: electric double-layer capacitors (EDLC) and pseudocapacitors or ultracapacitors [1, 4–6]. EDLC is based on the energy storage through accumulation of the charges at the interface of the electrode and the electrolyte. In EDLCs (which include carbon-based materials), have long-term stability and fast charge-discharge. In the second type of supercapacitor, i.e., pseudocapacitor, the energy is stored through redox or faradic reactions occurring between the electrode material and the electrolyte. Generally, pseudocapacitor electrodes include metal oxides and conducting polymers [7]. Among these, transition metal oxides are more advantageous because of low electrochemical series resistance (ESR), more valence states, long cycle life, etc.

Among transition metal oxides, iron oxides are of particular interest due to their easy synthesis, low cost, good structural stability and environmental friendliness. Iron oxides form an important class of materials that are ubiquitous in

nature from ancient times [8]. Because of the wide range of their physical and chemical properties, iron oxides are of great interest to a variety of scientific disciplines for various applications that range from opto-electronics, medicine, catalysis, corrosion protection, gas sensing, etc. [9, 10]. Among the different forms of iron oxides, hematite (α-Fe_2O_3) is the most common polymorph found naturally in soil and rocks because of its high thermodynamic stability and has lot of potential in these applications [11]. It is also one of the promising materials for supercapacitor applications as well [12].

Since supercapacitive performance of α-Fe_2O_3 depends on phase, crystallinity and morphology, different synthesis methods have been explored to get α-Fe_2O_3 nanostructures [13–24]. The present investigation aims for the synthesis of iron oxide films using liquid phase deposition (LPD) method to examine its utility as a supercapacitor. LPD is a process in which metal oxide or hydroxide thin films are formed on substrate through the ligand exchanging equilibrium reaction of the metal fluoro complex and the fluorine ion consumption reaction by addition of fluorine ion scavenger [25]. The LPD method has advantages such as easy and exact controllable ability of the thickness and dopant concentration. It is also simple, cost effective, energy efficient and can be used for larger substrates of complex shape [26]. Deki first attempted deposition of β-FeOOH and α-Fe_2O_3 thin films [27]. The β-FeOOH films deposited by using LPD method have been used in lithium-ion cells [28, 29]. In the present study, we have prepared hematite thin films by LPD method and studied their electrochemical properties for EC applications. To the best of our knowledge, this is for the first time we report the electrochemical properties of α-Fe_2O_3 thin films deposited by LPD method.

Experimental details

The deposition experiments were performed in open atmosphere at room temperature (300 K). Prior to deposition stainless steel (no-304), substrates (1 × 3 cm^2) were polished with zero grade polish paper and washed in detergent solution. These polished substrates were cleaned in 3% HCl for 1 min and then ultrasonically cleaned in double distilled water for 15 min. These cleaned stainless steel substrates were used for the deposition. FeOOH was precipitated from an aqueous solution of ferric nitrate [$Fe(NO_3)_3$] by using liquor ammonia. The precipitate was separated by filtration and washed repeatedly by using double distilled water and dried in air. The parent solution FeOOH-NH_4F.HF was obtained by dissolving requisite amount (to make concentration 1 M) of precipitate of FeOOH in 0.16 M ammonium bifluoride (NH_4F.HF) aqueous solution. Boric acid, H_3BO_3 (scavenging agent) solution of 1 M was added to this parent solution. Substrates were vertically suspended and soaked in the reaction solution for 20 h. After being removed from the reaction solution the films were rinsed with double distilled water and dried in open atmosphere. In case of LPD, the concentration of scavenging agent has significant influence on morphology of the deposited film [30]. It is noteworthy that supercapacitive performance also critically depends on the morphology of the electrode material [7, 8]. Considering this, we have deposited films by varying concentration of H_3BO_3. We found that the films deposited with 1 M boric acid exhibit maximum specific capacitance (Supporting fig. S_1) and hence used it for further studies. To ensure complete crystallization, the films were annealed at 500 °C in air for 1 h followed by natural cooling up to room temperature. These films were further used for characterization. The same deposition process was followed as mentioned above for glass substrates for optical studies. The thickness of the as-deposited film was ~760 nm, whereas after annealing it was reduced to ~500 nm due to removal of water content, phase transformation and crystallization after annealing.

Characterization techniques

Thermogravitometry analysis (TGA) and differential scanning calorimetry (DSC) of the powder (scratched from the as-deposited film) were investigated by using Mettler-Toledo TGA/DSC1 Star^e system. It was carried out from room temperature to 600 °C in air atmosphere with 8 °C/min heating rate in alumina crucible. The phase composition and structural characterization of as-deposited and annealed films were recorded using an X-ray diffractometer Bruker D8 Advance instrument in the 2θ range 20–80^0 scanned with CuK_α (λ = 1.54 Å) radiation. Raman spectra were measured on inVia Renishaw instrument in the wavenumber range 100–1000 cm^{-1} using He-Ne laser excitation source (632 nm, 6 mW) with resolution of 1 cm^{-1}. The surface morphology of the films was observed by using field emission scanning electron microscopy (FE-SEM) on Nova NanoSEM450. The wettability of the films was tested by measuring the contact angle (θ) of a water drop of volume 5 μl placed on the film surface using an optical contact angle goniometer (OCA) at room temperature. Optical properties of the films were studied by using JascoV-670 UV-Visible spectrophotometer in the wavelength range 200–800 nm.

Electrochemical characterizations

The cyclic voltammetry (CV), galvanostatic charge-discharge (GCD), electrochemical impedance spectroscopy (EIS) studies were carried out using a computer-controlled IVIUM 1A potentiostat with standard three electrodes system. Platinum wire was used as a counter electrode, whereas saturated Ag/AgCl was used as a reference electrode. The α-Fe_2O_3 (annealed) film deposited on stainless steel substrate acted as a working electrode. Previous electrochemical studies of iron oxides revealed that for obtaining the maximum specific

capacitance Na_2SO_3 electrolyte is better [31, 32, 20, 33–35, 13, 14, 18, 36, 23]. The cyclic voltammograms were recorded between −1.5 to 0.0 V potential window in electrolyte Na_2SO_3 aqueous solutions of different concentrations 0.025, 0.05, 0.5, 1 and 2 M for different scan rates from 5 to 200 mV s^{-1}. The area of the α-Fe_2O_3 electrode was (1 cm × 1 cm) and the weight of the active material dipped in the electrolyte was 0.3 mg, which was calculated by the weight difference method. The GCD and EIS studies were performed in 0.5 M Na_2SO_3 electrolyte, for which best supercapacitive performance was observed in cyclic voltammetry.

Results and discussion

Film formation and reaction mechanism

As proposed by Deki et al. [27] the mechanism of an iron oxyhydroxide film formation by LPD can be explained as follows. In the treatment solution Fe^{3+} ions are accompanied by F^- ions to give $[FeF_6]^{3-}$. F^-ions are released in reaction (1 and 2) and the reactions proceed resulting in the film formation.

$$[FeF_6]^{3-} + nH_2O \rightleftarrows \left[FeF_{6-n}(OH)_n\right]^{3-} + nHF \quad (1)$$

$$\left[FeF_{6-n}(OH)_n\right]^{3-} + nH_2O \rightleftarrows \left[Fe(OH)_6\right]^{3-} + nHF \quad (2)$$

$$H_3BO_3 + 4HF \rightleftarrows BF_4^- + H_3O^+ + 2H_2O \quad (3)$$

The ligand-exchange equilibrium reactions (hydrolysis of iron fluoro complex ions) (1 and 2) are shifted to right-hand side by the addition of boric acid to form stable complex ions as in reactions 1 and 3. The consumption of F^- ions occurs due to addition of boric acid (scavenging agent of F^- ions) to the treatment solution. This accelerates the ligand exchange of $[FeF_6]^{3-}$ and $[FeF_{6-n}(OH)_n]^{3-}$ as in reaction 1 and 2. The $[Fe(OH)_6]^{3-}$ formed in reaction (2) is then dehydrated on the surface of the substrate, which results in the formation of iron oxyhydroxide thin film.

Structural, morphological and wettability analysis

TGA

The decomposition and crystallization temperature of the as-deposited film was confirmed from TGA and DSC measurements as shown in Fig. 1a. A sharp endothermic peak in the DSC curve at 175 °C is seen due to the evaporation of physisorbed water molecules [37]. The second and third endothermic peaks in the DSC curve at 250 and 300 °C are due to the decomposition of FeOOH [38] and the removal of OH^-group [39], respectively. As seen in TGA curve, the as-deposited FeOOH mainly undergoes the weight loss in two steps. First, the weight loss of ~8% at 200 °C is attributed to the removal of adsorbed water. Second, the weight loss of 54% from 200 to 360 °C is assigned to the elimination of hydroxyl groups where the decomposition of FeOOH occurs, which is a typical endothermic reaction [39]. The weight loss ceases at ~500 °C and the mass remains same afterwards. The residue can be attributed to the thermodynamically stable hematite phase of iron oxide, α-Fe_2O_3 [38]. Taking into consideration the TGA results, we conclude that 500 °C is enough for phase conversion of FeOOH to hematite (α-Fe_2O_3) and hence in the present work the as-deposited films were annealed at 500 °C in air for 1 h in order to get crystalline hematite thin films.

XRD and Raman studies

The XRD measurements were performed to determine the crystal structure and the phase of the films. Figure 1b shows the XRD patterns of the as-deposited (A) and annealed (B) films. The peaks found in the XRD pattern of as-deposited film are assigned to FeOOH having orthorhombic crystal structure in correspondence with the Joint Committee on Powder Diffraction Standards (JCPDS), card no. 81-0462. The peaks of stainless steel substrate (denoted as SS in the pattern) are also visible may be due to small thickness of the film. After annealing at 500 °C, the FeOOH structure is destructed and gets transformed to α-Fe_2O_3. In contrast with earlier report [27] in which glass substrates were used, in present study the phase transformation of FeOOH to α-Fe_2O_3 is seen at lower temperature probably due to the difference in substrate and concentration of boric acid used. It can be seen from the figure that the crystallinity is improved as the film was annealed at 500 °C in air. The peaks found in the XRD pattern of the annealed film at 500 °C are assigned to α-Fe_2O_3 with rhombohedral crystal structure in correspondence with JCPDS card no. 33-0664. The average crystallite sizes of the as-deposited (FeOOH) and the annealed film (α-Fe_2O_3), calculated by the Debye Scherrer relation ($D = 0.9\,\lambda/\beta\cos\theta$) [40] are about 62 and 26 nm, respectively.

Figure 1c shows the Raman spectra of the as-deposited and the annealed films. In Raman spectra, all peaks for the as-deposited film can be attributed to β-FeOOH (akaganeite) [41]. The peaks for the annealed film (B) seen in Raman spectra at 226 and 498 cm^{-1} are assigned to A_{1g} mode, four peaks 244, 291, 412 and 614 cm^{-1} are assigned to E_g mode of α-Fe_2O_3 (hematite) [42–44]. The band at 662 cm^{-1} assigned to E_u mode is mostly reported for hematite due to the presence of residual Fe_3O_4 or disorder in crystal lattice [42, 45]. Thus, Raman spectroscopy results reveal that FeOOH (as-deposited film) is fully transformed to α-Fe_2O_3 (annealed film) in conformity with XRD results.

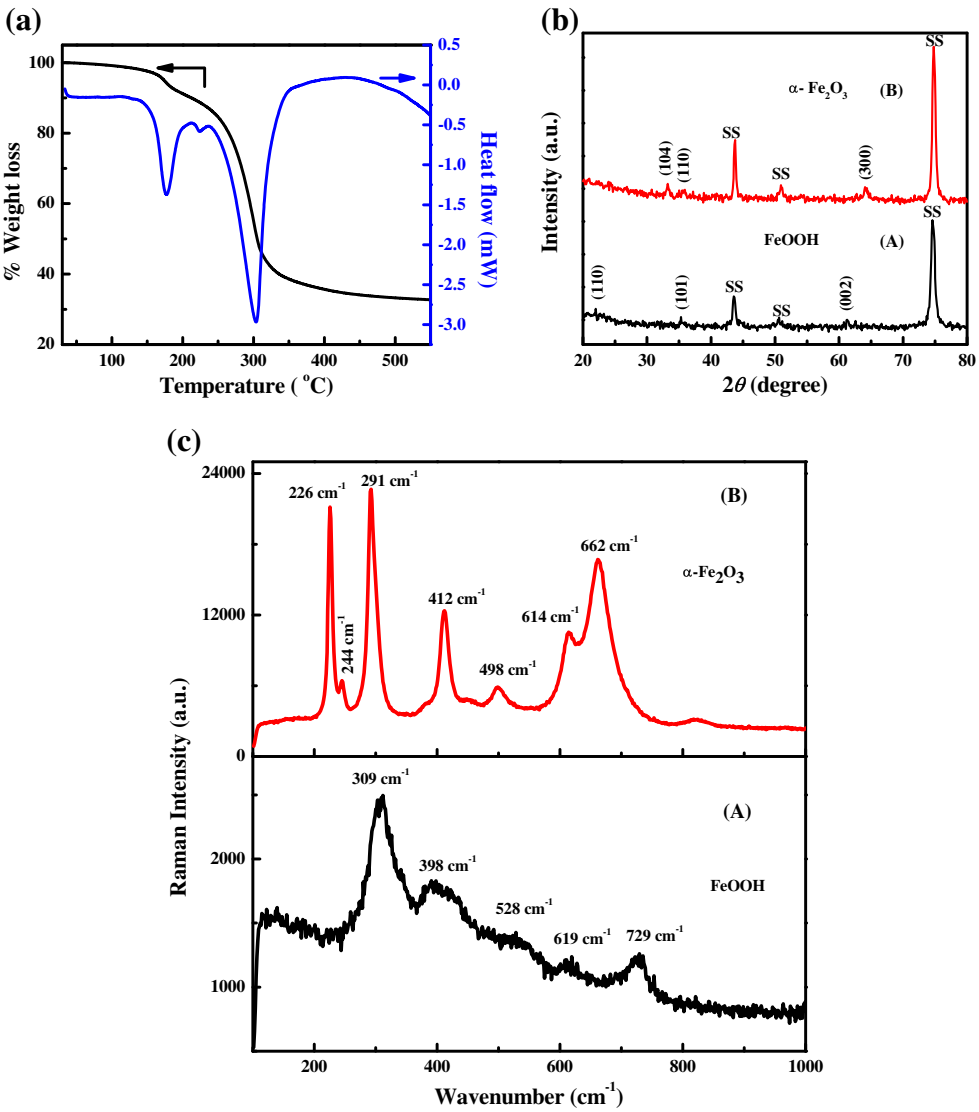

Fig. 1 **a** TGA–DSC curve of the as-deposited sample, **b** XRD pattern and **c** Raman spectra of the (*A*) as-deposited and (*B*) annealed films on stainless steel substrates, respectively

Morphology

Figure 2a, b shows the FE-SEM images of the as-deposited and the annealed films on stainless steel substrates. It can be seen from the micrographs that the compact film of spherically shaped densely packed particles are formed. After annealing the nature of the film is porous. In the as-deposited film ~10 at. % fluorine is present and after annealing it evaporated and became zero which may be the reason for the change in morphology from compact to porous (Supporting information fig. S_2(a, b)). Also, after annealing phase is changed to α-Fe_2O_3 from FeOOH as confirmed from XRD and Raman studies. For the as-deposited film cracks are seen (Supporting information fig. S_3(a)). This may be due to the internal stress of the film due to the contraction of the film upon drying [30]. After annealing at 500 °C, cracks are seen to increase (Supporting information fig. S_3(b)). During the annealing, shrinkage stress is generally dominant which could be the reason for the cracks [46]. The cracks may be useful for electrochemical supercapacitors study due to their high surface area [47, 48, 19, 49].

Wettability study

Surface wettability is examined to determine the nature (hydrophilic or hydrophobic) of the thin film surface as shown in Fig. 2c, d. The contact angle (θ) for the as-deposited film is 101° and that of the annealed film is 75°, suggesting that the surface of the film changes from hydrophobic to hydrophilic after annealing. The reason may be that the roughness became less after annealing of the film. The property of α-Fe_2O_3 film of being hydrophilic is useful in electrolyte/electrode interface for good performances in electrochemical supercapacitors [17].

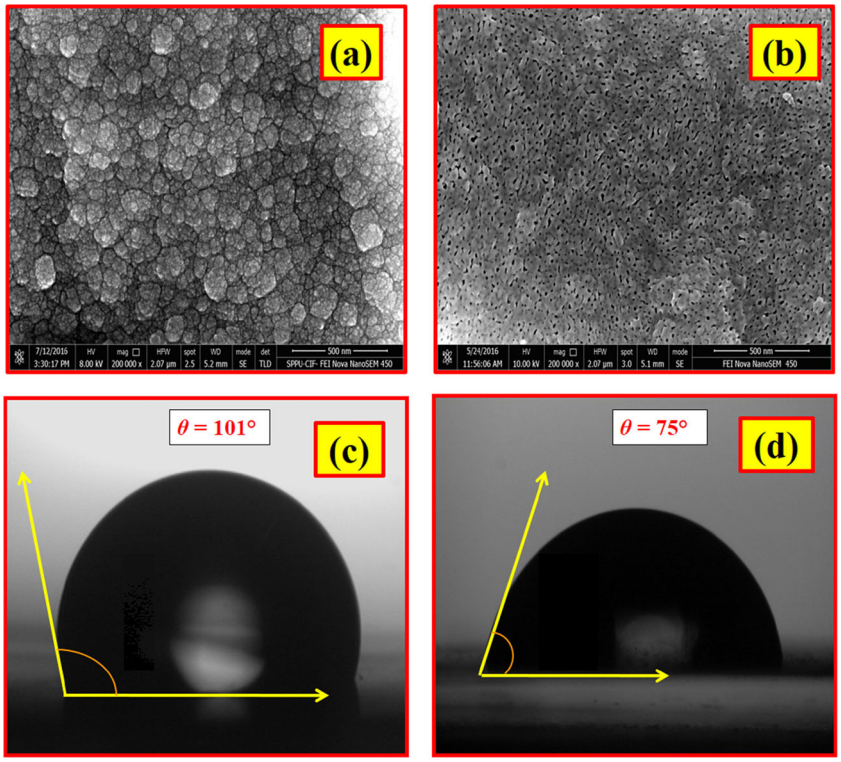

Fig. 2 FE-SEM micrographs **a, b** and water contact angle images **c, d** for the as-deposited and annealed films on stainless steel substrates, respectively

Optical properties

The variations in transmittance against wavelength for as-deposited and annealed films deposited on glass substrates are shown in Fig. 3a. The transmittance increases in visible range after 356 nm for as-deposited and around 393 nm for annealed films. The theory of optical absorption gives the relationship between the absorption coefficients α and the photon energy ($h\upsilon$),

$$\alpha = A\left(E_g - h\upsilon\right)^n / h\upsilon \quad (4)$$

where $h\upsilon$ is the photon energy, E_g is the optical band gap and A is the constant related to the effective masses associated with the valence and conduction bands. For direct allowed transition n = ½ and for allowed indirect transition n = 2 [50]. Figure 3b shows the variation of $(\alpha h\upsilon)^2$ with $h\upsilon$, which is a straight line in the domain of higher energies, indicating a direct optical transition. Equation (4) gives the band gap (E_g) when straight portion of plot is extrapolated to the point α = 0. The optical band gap of the FeOOH was found to be in the range 1.97 to 2.14 eV [51, 37, 52] and that of the α-Fe_2O_3 given in the literature data is 1.9–2.65 eV [53, 17, 54, 55]. The band gap obtained from Tauc-Mott plots (Fig. 3b) of FeOOH (as-deposited film) is 2.26 eV and that of α-Fe_2O_3 (annealed film at 500 °C) is 2.19 eV. Phase transition from FeOOH to α-Fe_2O_3 and increase in particle size may be responsible for decrease in the bandgap due to annealing.

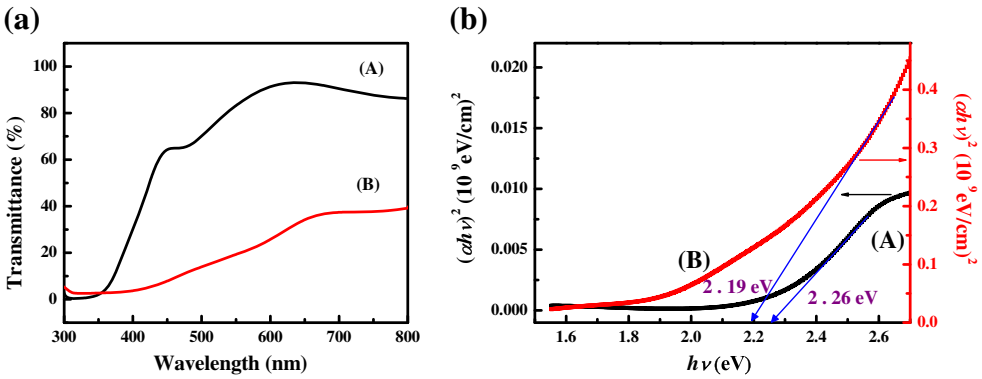

Fig. 3 **a** Variation of transmittance against wavelength and **b** variation of $(\alpha h\upsilon)^2$ against $(h\upsilon)$ for the (*A*) as-deposited and (*B*) annealed films on glass substrates, respectively

Electrochemical characterizations

Cyclic voltammetry (CV) studies

To determine the interfacial capacitance (*Ci*) and specific capacitance (*Cs*) cyclic voltammetry (CV) is usually preferred [56]. From CV curves, specific capacitance associated with the α-Fe_2O_3 electrode was calculated using the following relations (5, 6 and 7) [56, 57].

$$C = \int IdV/(V \times v) \tag{5}$$

$$Ci = C/A \tag{6}$$

$$Cs = Ci/m \tag{7}$$

where,

- I response current (mA),
- V potential window (V),
- v voltage scan rate (mV s^{-1}),
- Ci interfacial capacitance (F cm^{-2}),
- Cs specific capacitance (F g^{-1}),
- A electro-active area of the material dipped in the electrolyte (cm^2)
- m mass of the active electrode material dipped in the electrolyte (g).

The Fig. 4a, b, c, d, e shows CV curves of α-Fe_2O_3 electrode at scan rates 5–200 mV s^{-1} in Na_2SO_3 electrolyte of concentrations 0.025, 0.05, 0.5, 1 and 2 M. The shape of cyclic voltammograms suggests the pseudocapacitance characteristic of α-Fe_2O_3, which is distinguishable from rectangular shape of the electric double-layer capacitance [58]. The capacitance of α-Fe_2O_3 in Na_2SO_3 aqueous solution arises from the surface redox reaction of sulphur in the form of sulphate and sulphite anions [35]. The possible redox reaction between Fe (II) and Fe (III) is accompanied by adsorption of sulphite ions for charge balance on iron oxide [31, 33].

It can be seen from the CV curves that the area under the curve for different scan rates increases from the concentration 0.025 to 0.5 M of the electrolyte. This indicates that there is insufficiency of electrolyte ions to fully utilize the electroactive sites for 0.025 M. Further from 0.5 to 2 M, the area under the curve again decreases which reflects that 0.5 M concentration is sufficient to effectively use all the electroactive surface sites for charge storage. As seen in Fig. 4a, b, c, d, e current density increases with increasing scan rates [59]. It can be clearly seen from CV that there are distinct redox peaks during the anodic and cathodic sweeps [58]. From the Fig. 4a, b, c, d, e it is also observed that anodic peak positions shift towards higher potential with increase in scan rate. Accordingly, cathodic peak positions shift towards lower potential with increase in scan rate. It is noticed that the values of

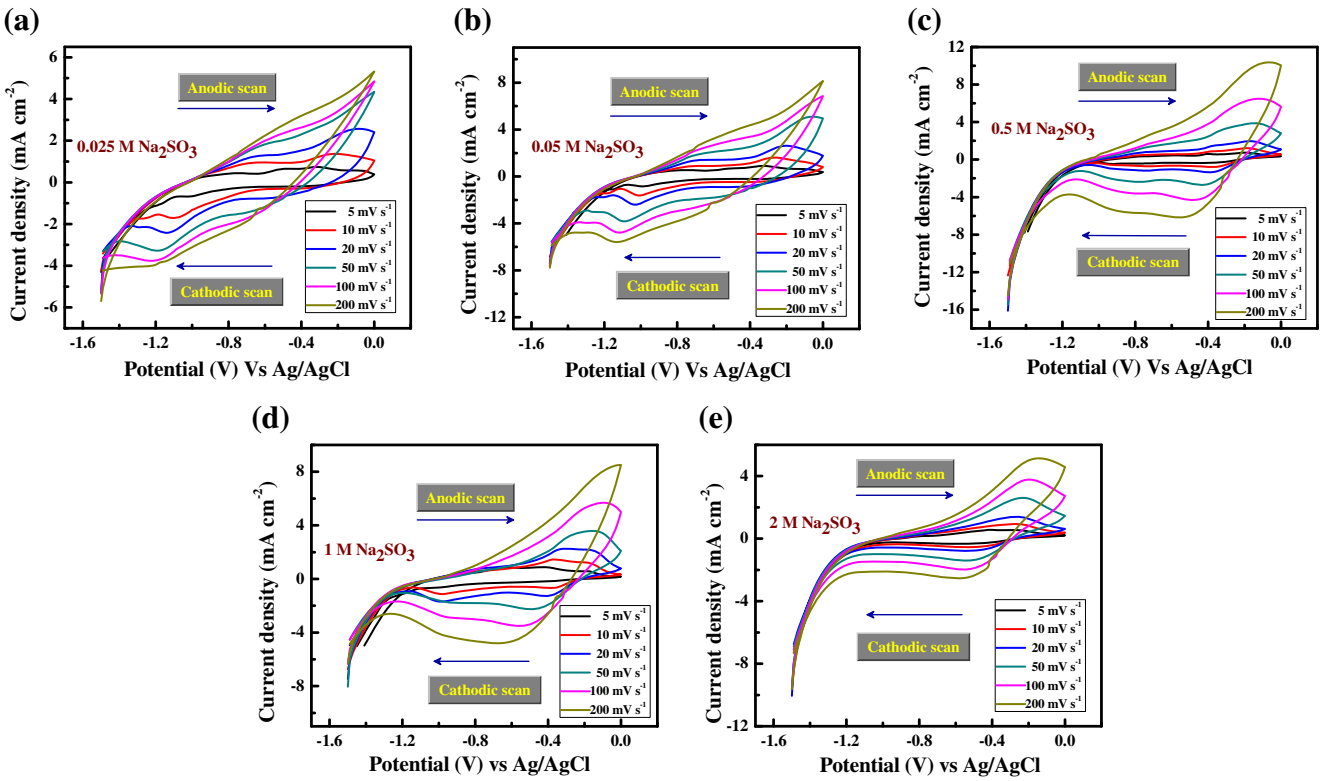

Fig. 4 **a**–**e** The CV curves of α-Fe_2O_3 electrode at the scan rates 5–200 mV s^{-1} in Na_2SO_3 electrolyte of concentrations **a** 0.025 M, **b** 0.05 M, **c** 0.5 M, **d** 1 M and **e** 2 M

Ci and *Cs* decrease with increase in scan rate (5–200 mV s^{-1}). The decrease in *Ci* and Cs can be attributed to the presence of inner active sites that cannot sustain the redox transitions completely at higher scan rates. At higher scan rates, ions do not have enough time to migrate in the double layer and hence the rate of double-layer formation slows down which results in decrease of *Cs* with increase in scan rate [60]. So, the *Cs* obtained at the slowest scan rate is believed to be the closest to that of full utilization of the electrode material [56, 61].

Figure 5a, b shows the variation of *Ci* and *Cs* with the concentration of the electrolyte for the scan rate 5–200 mV s^{-1}. It is seen that both *Ci* and *Cs* are increased from the concentration 0.025 to 0.5 M and then again decreases to 2 M concentration of the electrolyte at different scan rates. It is being reported that the electrolyte concentration has strong influence on the capacitance of a supercapacitor [62, 63]. The ion transport within the electrode layer is easier if the concentration of the electrolyte is high. But if the electrolyte concentration is too high, the ion transport may be reduced because of less water hydration and hence decrease in ion mobility. Thus, in the present study the optimized electrolyte concentration is found to be 0.5 M of Na_2SO_3 and the highest obtained values of *Ci* and *Cs* are 0.175 F cm^{-2} and 582 F g^{-1}, respectively at the scan rate 5 mV s^{-1} for 0.5 M aqueous Na_2SO_3 electrolyte. The *Cs* value obtained in the present work is higher than the reported values. The high value of specific capacitance may be attributed to the high surface area due to the porous nature of the film. The reported maximum values of *Cs* for α-Fe_2O_3 film electrode (binder-free) in different electrolytes calculated from the cyclic voltammograms are given in Table 1.

The importance of an electrochemical supercapacitor is examined by its stability and reversibility. As it is seen from the CV studies, the maximum specific capacitance was obtained at 0.5 M aqueous Na_2SO_3 solution and hence the electrochemical cyclic stability of the α-Fe_2O_3 electrode was tested in the same electrolyte up to 1000 cycles. Figure 6a shows the CV for 1st, 100th, 500th and 1000th cycles at the scan rate 100 mV s^{-1} in 0.5 M of aqueous Na_2SO_3. The area under the curve decreases up to 500th cycle and remains the same afterwards. In Fig. 6b, the variation of specific capacitance with cycle number for α-Fe_2O_3 electrode at 100 mV s^{-1} scan rate is shown. It is observed from the figure that initially capacitance decreases rapidly and then steadily with increasing cycle numbers. The decay in the value of capacitance may be due to dissolution of the electrode active material in the electrolyte and capacity imbalance between the electrodes which can cause the electrode potential unstable. As the wide potential window (−1.5 to 0 vs Ag/AgCl) [24] is used for cyclic voltammetry, well-defined redox peaks along with high specific capacitance are obtained but with the poor cycling stability [64–66, 12].

Galvanostatic charge-discharge studies

The galvanostatic charge-discharge curves of α-Fe_2O_3 film were recorded at different current densities of 2, 4, 6, 8 and 10 mA cm^{-2} in 0.5 M Na_2SO_3 electrolyte. The charge-discharge curves of α-Fe_2O_3 film are shown in Fig. 7a. The discharge curves can be divided into three linear regions. First linear region (V_1) represents the sudden *iR* drop in the potential range 0 to −0.24 V due to internal resistance of the α-Fe_2O_3 electrode [67]. Second linear region (V_2) shows the nearly linear portion of potential variation with time indicating the double-layer capacitance due to charge separation at the interface of the electrode and the electrolyte [68]. In third region (V_3) variation in slope of the potential with time curve is seen, that refers the pseudo-capacitive behaviour of the α-Fe_2O_3 electrode [57].

$$\mathrm{Cs} = (I \times t\mathrm{d}) \Big/ (V \times m) \tag{8}$$

$$\mathrm{SP} = (I \times V) \Big/ m \tag{9}$$

$$\mathrm{SE} = (I \times V \times t\mathrm{d}) \Big/ m \tag{10}$$

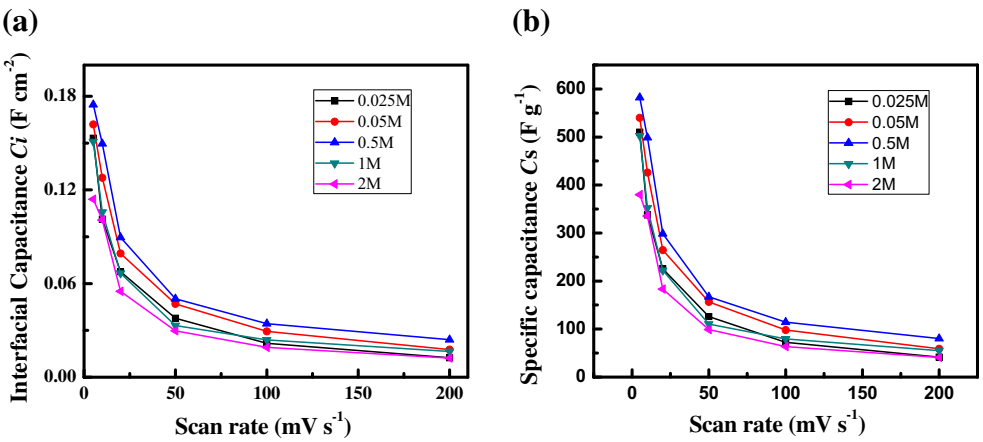

Fig. 5 **a** Scan rate effect on interfacial capacitance (*Ci*) and **b** scan rate effect on specific capacitance (*Cs*) of the α-Fe_2O_3 electrode at different concentrations of the electrolyte, respectively

Table 1 Supercapacitive performance of the α-Fe_2O_3 thin film electrode based on cyclic voltammetry

Sr. no.	Method of preparation of the α-Fe_2O_3 electrode	Electrolyte	Scan rate (mV s^{-1})	Maximum specific capacitance (F g^{-1})	Reference
1	Hydrothermal	3 M LiCl	10	64.5	[72]
2	Anodic deposition	1 M Li_2SO_4	5	146	[21]
3	SILAR	1 M NaOH	5	178	[17]
4	Electrospin	1 M LiOH	1	256	[15]
5	SILAR	1 M Na_2SO_4	5	283	[57]
6	SILAR	1 M Na_2SO_4	5	339	[73]
7	Spray processing	0.5 M Na_2SO_3	2	346	[14]
8	Spin coating	0.5 M Na_2SO_3	5	354.3	[18]
9	Electro-deposition	1 M KOH	5	487	[19]
10	LPD	0.5 M Na_2SO_3	5	582	Present work

where,

Cs specific capacitance (F g^{-1}),
I current density (mA cm^{-2}),
V potential window (V),
td discharging time (s),
m mass of the active material dipped in the electrolyte (g),
SP specific power (kW kg^{-1}),
SE specific energy (Wh kg^{-1}),

The specific capacitance, *C*s was calculated from the charge-discharge curves by the relation (8) [56, 61]. Figure 7b indicates the specific capacitance as a function of current densities of α-Fe_2O_3 film electrode. As current density increased from 2 to 10 mA cm^{-2}, the specific capacitance decreased from 179 to 142 F g^{-1}. The maximum *C*s value found is 179 F g^{-1} at current density 2 mA cm^{-2} which is consistent with the specific capacitance value 167 F g^{-1} obtained from CV curve at 50 mV s^{-1} in 0.5 M Na_2SO_3. Due to the fast charge transfer at the interface of the electrode and electrolyte, α-Fe_2O_3 electrode shows high capacitance at low current density. The *iR* drop increases with the increase in current density due to the ohmic resistance of the electrode [69]. The reported maximum values of Cs for α-Fe_2O_3 film electrode (binder-free) in different electrolytes calculated from the charge-discharge studies are given in Table 2. The specific power (*SP*) in kW $kg^{-1}$and the specific energy (*SE*) in Wh kg^{-1} were also calculated from the relations (9 and 10) [56, 60]. Figure 7c shows the plot for specific energy verses specific power (Ragone plot) of the α-Fe_2O_3 electrode. At current densities 2 to 10 mA cm^{-2} as the SP increases from 6.9 to 29.9 kW kg^{-1} the *SE* decreases from 53.4 to 31.8 Wh kg^{-1}, respectively.

Electrochemical impedance spectroscopy (EIS) study

A powerful technique to study the fundamental behaviour of an electrode material in an electrolyte is electrochemical impedance spectroscopy (EIS). The EIS measurements were carried out at room temperature to evaluate charge transfer resistance and phase angle. The Nyquist impedance plot of the α-Fe_2O_3 electrode was examined in the frequency range from 0.01 to 10^5 Hz of 0.01 V signal amplitude in 0.5 M Na_2SO_3 electrolyte as shown in Fig. 8a. Figure 8b displays the enlargement of the high frequency region and inset shows the equivalent circuit used to fit the Nyquist impedance plot. The

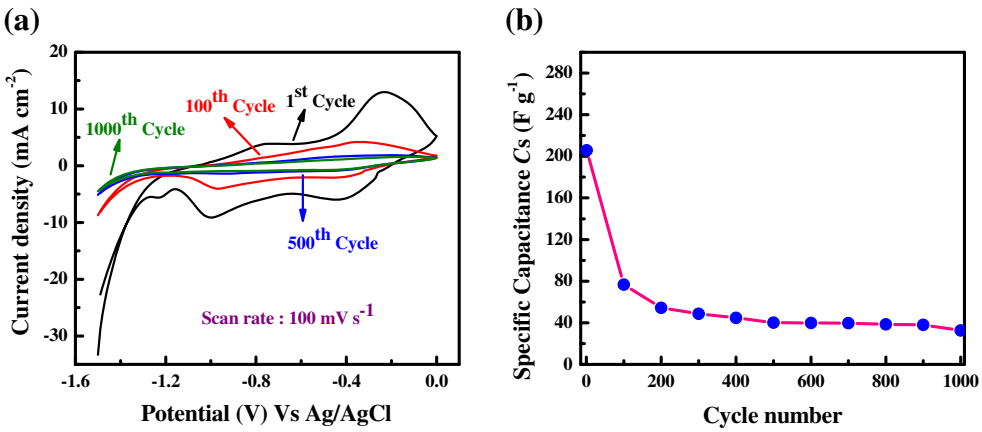

Fig. 6 **a** Electrochemical cyclic stability and **b** specific capacitance against cycle number of the α-Fe_2O_3 electrode at the scan rate 100 mV s^{-1}

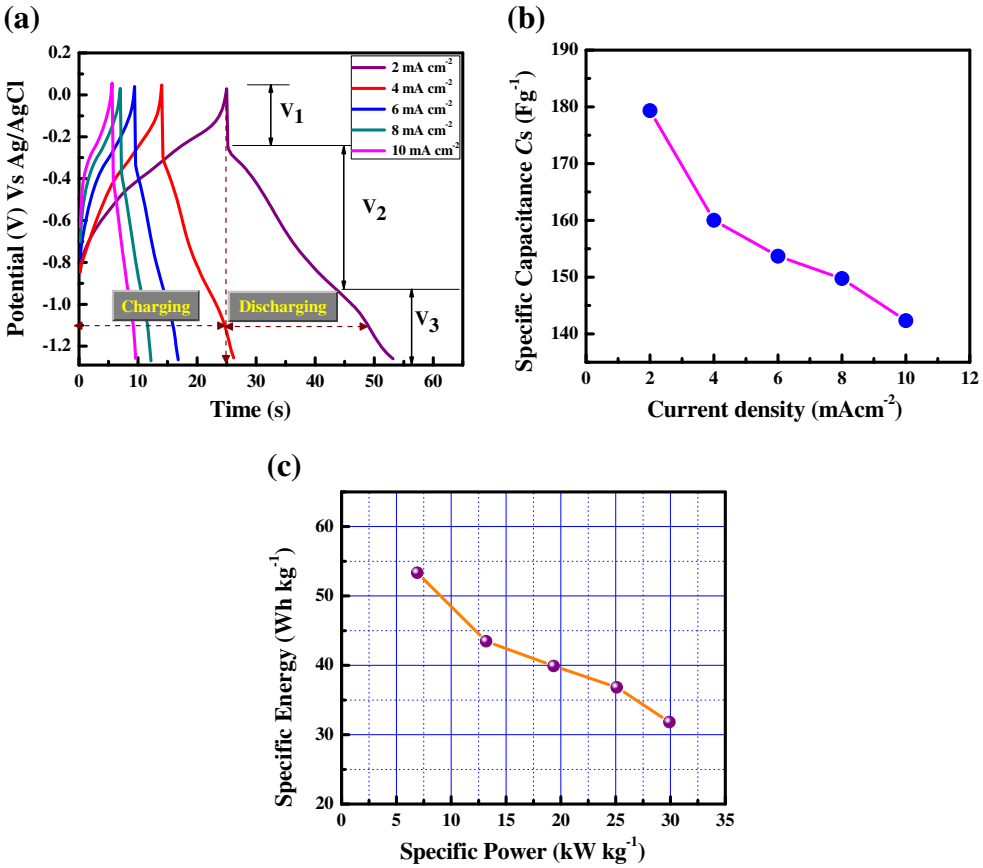

Fig. 7 **a** Galvanostatic charge-discharge curves at current densities 2, 4, 6, 8 and 10 mA cm^{-2}, **b** specific capacitance as a function of discharge current densities and **c** Ragone plot of the α-Fe_2O_3 electrode

equivalent circuit implies the best fitted impedance data of the α-Fe_2O_3 electrode.

The imaginary part of the impedance spectrum sharply increases in lower frequency region indicating the supercapacitive behaviour of the α-Fe_2O_3 electrode [57]. Nature of the plot was studied at the beginning of the semicircle (high-frequency region) because of the resistance of the electrolyte (R_s = 22 Ω) is independent of the frequency. R_{ct} is the charge transfer resistance, which was found to be 18 Ω. The equivalent series resistance (ESR) obtained was 40 Ω. In the intermediate region of frequency, it is noticed that the Nyquist plot intersects the real axis (Z') at ~45° angle is due to the Warburg (W) component, which is the characteristic of ion diffusion into the electrode materials [70]. In the low frequency part, the straight line bends more towards the imaginary axis which indicates the good capacitive behaviour of the

Table 2 Preparation and supercapacitive performance of the α-Fe_2O_3 thin film electrode based on charge-discharge studies

Sr. no.	Method of preparation of the α-Fe_2O_3 electrode	Electrolyte	Current density	Maximum specific capacitance (F g^{-1})	Reference
1	Hydrothermal	3 M LiCl	0.5 mA cm^{-2}	89	[72]
2	Anodization	1 M Li_2SO_4	1 mA cm^{-2}	138	[22]
3	Template-free process	1 M Li_2SO_4	0.36 Ag^{-1}	147	[16]
4	LPD	0.5 M Na_2SO_3	2 mA cm^{-2}	179	Present work
5	Spray processing	0.5 M Na_2SO_3	2 Ag^{-1}	213	[14]
6	Electrospin	1 M LiOH	5 Ag^{-1}	348	[15]
7	SILAR	1 M Na_2SO_4	1 mA cm^{-2}	360	[73]
8	Spin coating	0.5 M Na_2SO_3	3 Ag^{-1}	365.7	[18]
9	Electrodeposition	1 M KOH	2.5 Ag^{-1}	540	[48]

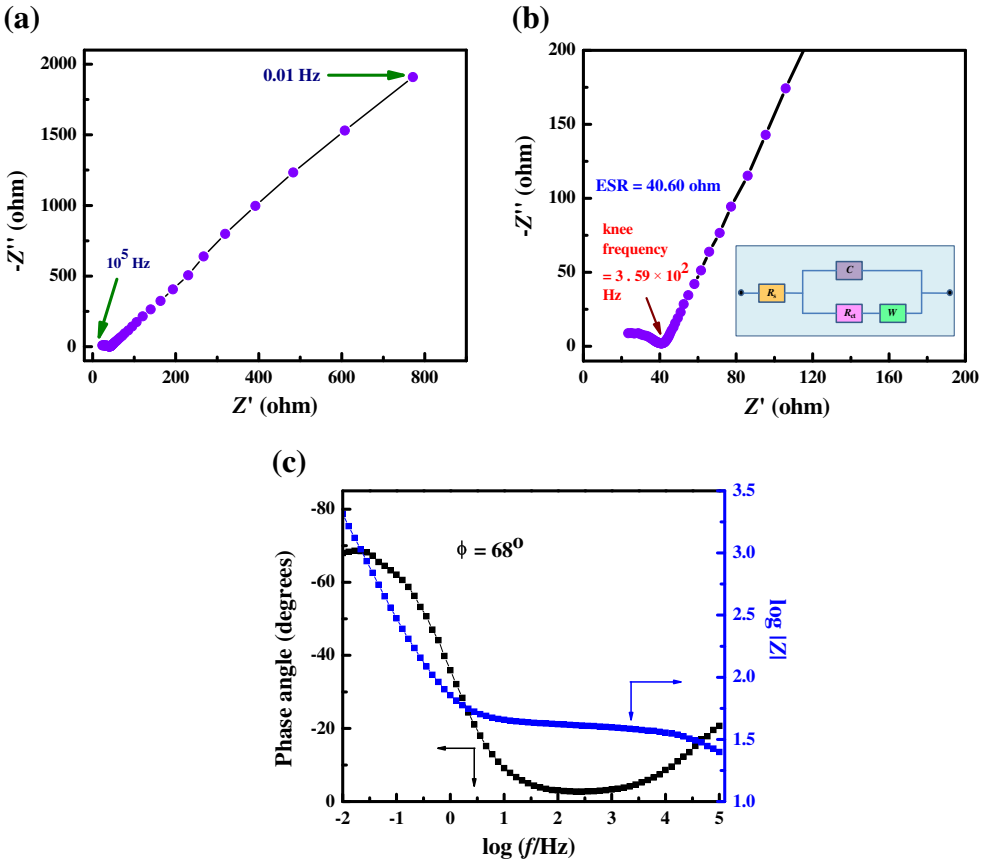

Fig. 8 **a** Nyquist impedance plot (*Z*" against *Z*') in the frequency range 10^5–0.01 Hz, **b** enlarged high-frequency region of Nyquist impedance plot (*inset* shows the equivalent circuit to fit the electrochemical impedance spectroscopy) and **c** bode plot of phase angle (φ) and log |*Z*| against log (*f*/*Hz*) of α-Fe_2O_3 electrode

electrode material [71]. Relaxation time constant (τ) was estimated using the expression (11) [70],

$$\tau = 1 \Big/ (2 \times \pi \times f) \tag{11}$$

where,

τ relaxation time constant (s),
f frequency corresponding to the maximum imaginary (*Z*") component of the semicircle (Hz).

The calculated relaxation time (τ) was 26 ms, indicating low relaxation time constant ensuring characteristic property of fast charging-discharging of a supercapacitor. Also, the smaller τ of α-Fe_2O_3 electrode provides high power density due to the capability of faster energy release [70]. Figure 8c shows bode plot of α-Fe_2O_3 electrode. The phase angle of α-Fe_2O_3 electrode was about 68° at low frequency (0.017 Hz) which corresponds to contribution of capacitance from pseudocapacitance. The phase angle increases with decrease in frequency. This angle approaches towards 90° and hence the α-Fe_2O_3 electrode behaves more like a capacitor [70].

Conclusion

In summary, α-Fe_2O_3 films have been successfully deposited on stainless steel substrates by liquid phase deposition (LPD) method followed by annealing. The XRD and Raman studies reveal the complete phase formation to α-Fe_2O_3 thin films after annealing at 500 °C. FE-SEM images show the change in morphology from compact to porous after annealing. The wettability test reveals that due to annealing, the hydrophobic film was transformed to hydrophilic. The highest obtained value of specific capacitance found from cyclic voltammetry was 582 Fg^{-1} at 5 mV s^{-1} in 0.5 M Na_2SO_3 electrolyte. The maximum value of specific capacitance was 179 F g^{-1} from the charge-discharge curve at the current density 2 mA cm^{-2}. The equivalent series resistance (ESR) obtained from Nyquist plot is 40 Ω. Hence, the results obtained reveal that the α-Fe_2O_3 films prepared by LPD method are affordable and have great potential application as a low cost option for supercapacitor.

Acknowledgements The authors are thankful to DRDP and UPE programs of Savitribai Phule Pune University, Pune, India for their financial support. The authors would like to thank Dr. Arun G. Banpurkar for contact angle measurements. The electrochemical measurements were performed on IVIUM vertex 1A potentiostat/galvanostat donated by Alexander von Humboldt foundation, Germany.

References

1. Conway BE (1999) Electrochemical supercapacitors: scientific fundamentals and technological applications. Springer, US
2. Snook GA, Kao P, Best AS (2011) Conducting-polymer-based supercapacitor devices and electrodes. J Power Sources 196(1):1–12
3. Zhang LL, Zhao XS (2009) Carbon-based materials as supercapacitor electrodes. Chem Soc Rev 38(9):2520–2531
4. Salunkhe RR, Kamachi Y, Torad NL, Hwang SM, Sun Z, Dou SX, Kim JH, Yamauchi Y (2014) Fabrication of symmetric supercapacitors based on MOF-derived nanoporous carbons. J Mater Chem A 2(46):19848–19854
5. Salunkhe RR, Lee YH, Chang KH, Li JM, Simon P, Tang J, Torad NL, Hu CC, Yamauchi Y (2014) Nanoarchitectured graphene-based supercapacitors for next-generation energy-storage applications. Chemistry 20(43):13838–13852
6. Tang J, Salunkhe RR, Liu J, Torad NL, Imura M, Furukawa S, Yamauchi Y (2015) Thermal conversion of core-shell metal-organic frameworks: a new method for selectively functionalized nanoporous hybrid carbon. J Am Chem Soc 137(4):1572–1580
7. Lokhande CD, Dubal DP, Joo O-S (2011) Metal oxide thin film based supercapacitors. Curr Appl Phys 11(3):255–270
8. Fisher RA, Watt MR, Ready WJ (2013) Functionalized carbon nanotube supercapacitor electrodes: a review on pseudocapacitive materials. ECS Journal of Solid State Science and Technology 2(10):M3170–M3177
9. Wu W, Wu Z, Yu T, Jiang C, Kim W-S (2016) Recent progress on magnetic iron oxide nanoparticles: synthesis, surface functional strategies and biomedical applications. Sci Technol Adv Mater 16(2):023501
10. Xu P, Zeng GM, Huang DL, Feng CL, Hu S, Zhao MH, Lai C, Wei Z, Huang C, Xie GX, Liu ZF (2012) Use of iron oxide nanomaterials in wastewater treatment: a review. Sci Total Environ 424:1–10
11. Jubb AM, Allen HC (2010) Vibrational spectroscopic characterization of hematite, Maghemite, and magnetite thin films produced by vapor deposition. Acs Appl Mater Inter 2(10):2804–2812
12. Xia Q, Xu M, Xia H, Xie J (2016) Nanostructured iron oxide/hydroxide-based electrode materials for supercapacitors. ChemNanoMat 2(7):588–600
13. Abdi A, Trari M (2013) Investigation on photoelectrochemical and pseudo-capacitance properties of the non-stoichiometric hematite α-Fe2O3 elaborated by sol–gel. Electrochim Acta 111:869–875
14. Fu C, Mahadevegowda A, Grant PS (2016) Production of hollow and porous Fe2O3from industrial mill scale and its potential for large-scale electrochemical energy storage applications. J Mater Chem A 4(7):2597–2604
15. Binitha G, Soumya MS, Madhavan AA, Praveen P, Balakrishnan A, Subramanian KRV, Reddy MV, Nair SV, Nair AS, Sivakumar N (2013) Electrospun α-Fe2O3 nanostructures for supercapacitor applications. J Mater Chem A 1(38):11698
16. Huang JC, Yang SN, Xu Y, Zhou XB, Jiang X, Shi NN, Cao DX, Yin JL, Wang GL (2014) Fe2O3 sheets grown on nickel foam as electrode material for electrochemical capacitors. J Electroanal Chem 713:98–102
17. Kulal PM, Dubal DP, Lokhande CD, Fulari VJ (2011) Chemical synthesis of Fe2O3 thin films for supercapacitor application. J Alloy Compd 509(5):2567–2571
18. Liu J, Lee E, Kim YT, Kwon YU (2014) Ultra-high capacitance hematite thin films with controlled nanoscopic morphologies. Nanoscale 6(18):10643–10649
19. Lokhande BJ, Ambare RC, Bharadwaj SR (2014) Thermal optimization and supercapacitive application of electrodeposited Fe2O3 thin films. Measurement 47:427–432
20. Shivakumara S, Penki TR, Munichandraiah N (2013) Synthesis and characterization of porous flowerlike -Fe2O3 nanostructures for supercapacitor application. ECS Electrochemistry Letters 2(7): A60–A62
21. Wu MS, Lee RH (2009) Electrochemical growth of iron oxide thin films with nanorods and nanosheets for capacitors. J Electrochem Soc 156(9):A737–A743
22. Xie KY, Li J, Lai YQ, Lu W, Zhang ZA, Liu YX, Zhou LM, Huang HT (2011) Highly ordered iron oxide nanotube arrays as electrodes for electrochemical energy storage. Electrochem Commun 13(6): 657–660
23. Yousefi T, Golikand AN, Mashhadizadeh MH (2013) Synthesis of iron oxide nanoparticles at low bath temperature: characterization and energy storage studies. Mater Sci Semicond Process 16(6): 1837–1841
24. Zhang M, Chen K, Chen X, Peng X, Sun X, Xue D (2015) Ethylenediamine-assisted crystallization of Fe2O3 microspindles with controllable size and their pseudocapacitance performance. CrystEngComm 17(7):1521–1525
25. Parikh H, De Guire MR (2009) Recent progress in the synthesis of oxide films from liquid solutions. J Ceram Soc Jpn 117(1363):228–235
26. Ko HYY, Mizuhata M, Kajinami A, Deki S (2005) The dispersion of Au nanoparticles in SiO2/TiO2 layered films by the liquid phase deposition (LPD) method. Thin Solid Films 491(1–2):86–90
27. Deki S, Aoi Y, Okibe J, Yanagimoto H, Kajinami A, Mizuhata M (1997) Preparation and characterization of iron oxyhydroxide and iron oxide thin films by liquid-phase deposition. J Mater Chem 7(9):1769–1772
28. Tabuchi T, Katayama Y, Nukuda T, Ogumi Z (2009) Surface reaction of β-FeOOH film negative electrode for lithium-ion cells. J Power Sources 191(2):636–639
29. Tabuchi T, Katayama Y, Nukuda T, Ogumi Z (2009) β-FeOOH thin film as positive electrode for lithium-ion cells. J Power Sources 191(2):640–643
30. Deki S, Yoshida N, Hiroe Y, Akamatsu K, Mizuhata M, Kajinami A (2002) Growth of metal oxide thin films from aqueous solution by liquid phase deposition method. Solid State Ionics 151(1–4):1–9
31. Chen J, Huang KL, Liu SQ (2009) Hydrothermal preparation of octadecahedron Fe3O4 thin film for use in an electrochemical supercapacitor. Electrochim Acta 55(1):1–5
32. Nagarajan N, Zhitomirsky I (2006) Cathodic electrosynthesis of iron oxide films for electrochemical supercapacitors. J Appl Electrochem 36(12):1399–1405
33. Wang SY, Ho KC, Kuo SL, Wu NL (2006) Investigation on capacitance mechanisms of Fe3O4 electrochemical capacitors. J Electrochem Soc 153(1):A75–A80
34. Wang SY, Wu NL (2003) Operating characteristics of aqueous magnetite electrochemical capacitors. J Appl Electrochem 33(3–4): 345–348
35. Wu NL, Wang SY, Han CY, Wu DS, Shiue LR (2003) Electrochemical capacitor of magnetite in aqueous electrolytes. J Power Sources 113(1):173–178
36. Shivakumara S, Penki TR, Munichandraiah N (2013) Preparation and electrochemical performance of porous hematite (α-Fe2O3) nanostructures as supercapacitor electrode material. J Solid State Electrochem 18(4):1057–1066
37. Parameshwari R, Priyadarshini P, Chandrasekaran G (2011) Optimization, structural, spectroscopic and magnetic studies on stable akaganeite nanoparticles via co-precipitation method. American Journal of Materials Science 1(1):18–25
38. Song YQ, Qin SS, Zhang YW, Gao WQ, Liu JP (2010) Large-scale porous hematite nanorod arrays: direct growth on titanium foil and reversible lithium storage. J Phys Chem C 114(49):21158–21164
39. Lu J, Chen D, Jiao X (2006) Fabrication, characterization, and formation mechanism of hollow spindle-like hematite via a solvothermal process. J Colloid Interface Sci 303(2):437–443

40. Sartale SD, Ansari AA, Rezvani SJ (2013) Influence of Ti film thickness and oxidation temperature on TiO2 thin film formation via thermal oxidation of sputtered Ti film. Mater Sci Semicond Process 16(6):2005–2012
41. Colomban P, Cherifi S, Despert G (2008) Raman identification of corrosion products on automotive galvanized steel sheets. J Raman Spectrosc 39(7):881–886
42. Bersani D, Lottici PP, Montenero A (1999) Micro-Raman investigation of iron oxide films and powders produced by sol-gel syntheses. J Raman Spectrosc 30(5):355–360
43. Tahir AA, Wijayantha KGU, Saremi-Yarahmadi S, Mazhar M, McKee V (2009) Nanostructured α-Fe2O3Thin films for photoelectrochemical hydrogen generation. Chem Mater 21(16): 3763–3772
44. Nieuwoudt MK, Comins JD, Cukrowski I (2011) The growth of the passive film on iron in 0.05 M NaOH studied in situ by Raman micro-spectroscopy and electrochemical polarisation. Part I: near-resonance enhancement of the Raman spectra of iron oxide and oxyhydroxide compounds. J Raman Spectrosc 42(6):1335–1339
45. Cesar I, Sivula K, Kay A, Zboril R, Graetzel M (2009) Influence of feature size, film thickness, and silicon doping on the performance of nanostructured hematite photoanodes for solar water splitting. J Phys Chem C 113(2):772–782
46. Lee MT, Chang JK, Hsieh YT, Tsai WT (2008) Annealed Mn-Fe binary oxides for supercapacitor applications. J Power Sources 185(2):1550–1556
47. Qing XX, Liu SQ, Huang KL, Lv KZ, Yang YP, Lu ZG, Fang D, Liang XX (2011) Facile synthesis of Co3O4 nanoflowers grown on Ni foam with superior electrochemical performance. Electrochim Acta 56(14):4985–4991
48. Lokhande BJ, Ambare RC, Mane RS, Bharadwaj SR (2013) Concentration-dependent electrochemical supercapacitive performance of Fe2O3. Curr Appl Phys 13(6):985–989
49. Suhasini (2013) Effect of deposition method and the surfactant on high capacitance of electrochemically deposited MnO2 on stainless steel substrate. J Electroanal Chem 690:13–18
50. Sartale SD, Lokhande CD (2000) Growth of copper sulphide thin films by successive ionic layer adsorption and reaction (SILAR) method. Mater Chem Phys 65(1):63–67
51. Mohapatra M, Mohapatra L, Anand S, Mishra BK (2010) One-pot synthesis of high surface area nano-akaganeite powder and its cation sorption behavior. J Chem Eng Data 55(4):1486–1491
52. Xiong Y, Xie Y, Chen S, Li Z (2003) Fabrication of self-supported patterns of aligned beta-FeOOH nanowires by a low-temperature solution reaction. Chemistry 9(20):4991–4996
53. Barik R, Mohapatra M (2015) Solvent mediated surface engineering of α-Fe2O3nanomaterials: facet sensitive energy storage materials. CrystEngComm 17(47):9203–9215
54. Mallick P, Dash BN (2013) X-ray diffraction and UV-visible characterizations of α-Fe2O3 nanoparticles annealed at different temperature. Nanosci Nanotechnol 3(5):130–134
55. Schrebler R, Bello K, Vera F, Cury P, Muñoz E, del Río R, Gómez Meier H, Córdova R, Dalchiele EA (2006) An electrochemical deposition route for obtaining α-Fe[sub 2]O[sub 3] thin films. Electrochem Solid-State Lett 9(7):C110–C113
56. Chen SM, Ramachandran R, Mani V, Saraswathi R (2014) Recent advancements in electrode materials for the high-performance electrochemical supercapacitors: a review. Int J Electrochem Sc 9(8): 4072–4085
57. Gund GS, Dubal DP, Chodankar NR, Cho JY, Gomez-Romero P, Park C, Lokhande CD (2015) Low-cost flexible supercapacitors with high-energy density based on nanostructured MnO2 and Fe2O3 thin films directly fabricated onto stainless steel. Scientific reports 5:12454
58. Zhu MY, Wang Y, Meng DH, Qin XZ, Diao GW (2012) Hydrothermal synthesis of hematite nanoparticles and their electrochemical properties. J Phys Chem C 116(30):16276–16285
59. Deshmukh PR, Bulakhe RN, Pusawale SN, Sartale SD, Lokhande CD (2015) Polyaniline-RuO2 composite for high performance supercapacitors: chemical synthesis and properties. RSC Adv 5(36):28687–28695
60. Patil SJ, Lokhande CD (2015) Fabrication and performance evaluation of rare earth lanthanum sulfide film for supercapacitor application: effect of air annealing. Mater Design 87:939–948
61. Deshmukh PR, Patil SV, Bulakhe RN, Sartale SD, Lokhande CD (2014) Inexpensive synthesis route of porous polyaniline-ruthenium oxide composite for supercapacitor application. Chem Eng J 257:82–89
62. Zheng JP (1997) The effect of salt concentration in electrolytes on the maximum energy storage for double layer capacitors. J Electrochem Soc 144(7):2417–2420
63. Tsay KC, Zhang L, Zhang JJ (2012) Effects of electrode layer composition/thickness and electrolyte concentration on both specific capacitance and energy density of supercapacitor. Electrochim Acta 60:428–436
64. Cheng X, Gui X, Lin Z, Zheng Y, Liu M, Zhan R, Zhu Y, Tang Z (2015) Three-dimensional α-Fe2O3/carbon nanotube sponges as flexible supercapacitor electrodes. J Mater Chem A 3(42):20927–20934
65. Liu J, Zheng M, Shi X, Zeng H, Xia H (2016) Amorphous FeOOH quantum dots assembled mesoporous film anchored on graphene Nanosheets with superior electrochemical performance for supercapacitors. Adv Funct Mater 26(6):919–930
66. Wang L, Ji H, Wang S, Kong L, Jiang X, Yang G (2013) Preparation of Fe3O4 with high specific surface area and improved capacitance as a supercapacitor. Nanoscale 5(9):3793–3799
67. Naveen AN, Selladurai S (2014) Investigation on physiochemical properties of Mn substituted spinel cobalt oxide for supercapacitor applications. Electrochim Acta 125:404–414
68. Patil SJ, Patil BH, Bulakhe RN, Lokhande CD (2014) Electrochemical performance of a portable asymmetric supercapacitor device based on cinnamon-like La2Te3 prepared by a chemical synthesis route. RSC Adv 4(99):56332–56341
69. Vu A, Li X, Phillips J, Han A, Smyrl WH, Bühlmann P, Stein A (2013) Three-dimensionally ordered mesoporous (3DOm) carbon materials as electrodes for electrochemical double-layer capacitors with ionic liquid electrolytes. Chem Mater 25(21):4137–4148
70. Patil SJ, Kumbhar VS, Patil BH, Bulakhe RN, Lokhande CD (2014) Chemical synthesis of α-La2S3 thin film as an advanced electrode material for supercapacitor application. J Alloy Compd 611:191–196
71. Li YH, Huang KL, Yao ZF, Liu SQ, Qing XX (2011) Co3O4 thin film prepared by a chemical bath deposition for electrochemical capacitors. Electrochim Acta 56(5):2140–2144
72. Lu X, Zeng Y, Yu M, Zhai T, Liang C, Xie S, Balogun MS, Tong Y (2014) Oxygen-deficient hematite nanorods as high-performance and novel negative electrodes for flexible asymmetric supercapacitors. Adv Mater 26(19):3148–3155
73. Chodankar NR, Dubal DP, Gund GS, Lokhande CD (2015) Bendable All-Solid-State Asymmetric Supercapacitors based on MnO2and Fe2O3 Thin Films. Energy Technology 3(6):625–631